The Mechanism of Brittle Fracture in a Microalloyed Steel: Part II. Mechanistic Modeling

D.P. FAIRCHILD, D.G. HOWDEN, and W.A.T. CLARK

In Part I of this study, cuboidally shaped inclusions were found to be responsible for cleavage initiation in a low-carbon, microalloyed steel. In Part II, electron microdiffraction was used to identify these inclusions as the fcc phase (NaCl prototype) in the titanium-nitrogen system. A model for cleavage as induced by these inclusions is proposed. A microcrack begins on one side of the TiN inclusion, propagates to the other side, and then transfers into the matrix. Initiation at a particular location in the particle is believed to be caused by dislocation pileup impingement and stress concentrations such as crystal defects and surface irregularities within the TiN. Dislocations in the TiN inclusions were imaged by transmission electron microscopy (TEM). After the TiN microcrack transfers into the matrix, propagation spreads radially. From the area of crack transfer, two simultaneous propagation paths reverse directions and rotate around the particle. The particle separates these cracks for a short distance, they travel on different cleavage planes, and upon rejoining, a ridge of torn matrix is created. The location of this ridge can be used to infer where cleavage began in the TiN and where the microcrack transferred into the matrix. Tessellated residual stresses arising from differential thermal contraction between the TiN and the matrix are suggested to increase the cleavage-initiating potency of TiN inclusions.

I. INTRODUCTION

IN Part I of this study,[1] the base-metal and weld heat-affected zone (HAZ) cleavage-fracture resistance of two microalloyed steels was investigated, and it was determined that one of them (steel B) had significantly lower toughness. Scanning electron fractography revealed that the toughness degradation was caused by cuboidal or angular-shaped, nonmetallic inclusions that acted as cleavage initiators. These inclusions were tentatively identified as TiN. It was surmised that these inclusions were particularly potent initiators because they were well bonded to the ferrite matrix.

The current article describes additional work on steel B, including chemical and structural characterization of the offending inclusions, fracture-specimen analysis, and scanning electron fractography. These results are combined with existing micromechanical cleavage models to produce a specific model of cleavage fracture in steel B.

In developing a cleavage model for steel B, particular emphasis is given to the physical phenomena influencing the instant of initiation. With respect to cleavage fracture in steel, at one moment the component is a relatively flawless continuum, then, an instant later, it is severed into two or more pieces. Given these bounding observations, it can be reasoned that, at a single instant in time, something within the microstructure, some tiny constituent, snaps first. The metallurgical feature that is first to break, the forces which cause it to break, and how its failure causes the entire component to fail catastrophically are among the subjects addressed.

D.P. FAIRCHILD, formerly Graduate Fellow, The Ohio State University, is Research Specialist with Exxon Production Research Co., Houston, TX 77252. D.G. HOWDEN, Associate Professor, Department of Industrial, Welding, and Systems Engineering, and W.A.T. CLARK, Professor, Department of Materials Science and Engineering, and Associate Dean, Graduate School, are with The Ohio State University, Columbus, OH 43210.

Manuscript submitted November 25, 1998.

II. BACKGROUND: CLEAVAGE FRACTURE IN STEELS

A. *Early Cleavage Modeling*

The topic of cleavage fracture is often introduced by discussing the theoretical strength of a solid. This strength can be estimated using the force-displacement laws governing the attractions between the atoms.[2,3] Conceptually, adjacent atomic planes are forced apart until new, free surfaces are created. Calculated strengths are up to 1000 times greater than those actually observed. However, engineering materials are not an ideal continuum of atoms. They contain minute discontinuities such as dislocations, grain boundaries, and second-phase particles. Under applied loads, these elements create local stress elevations that eventually cause some microstructural feature to break. This is the moment of cleavage initiation, and this minute crack may propagate to cause complete failure of the component.

Griffith[4] was perhaps first to quantify that tiny stress concentrations can cause cleavage in materials at loads well below their theoretical strength. Although Griffith correctly highlighted the importance of microcracks, his theory cannot be directly applied to most metals.[5,6,7] According to Griffith's law, cleavage-initiating microcracks in many metals should be about 1 or 2 μm in size. However, significant populations of such microcracks do not exist in well-manufactured engineering components; ones that *do* fail by cleavage. Griffith's theory did not address how cleavage could operate in a material that was initially defect free.

Approximately 30 years after Griffith's insights, and influenced by early studies on dislocation theory, it was reasoned that a microstructure, in reaction to the applied loads, would self-generate the critical flaws. Zener,[8] Mott,[9] and Stroh[7,10,11] (among others) contributed to the model shown in Figure 1, which depicts microcrack formation at the head of a dislocation pileup. By this mechanism, cleavage, a notably brittle event, is preceded by local slip deformation.

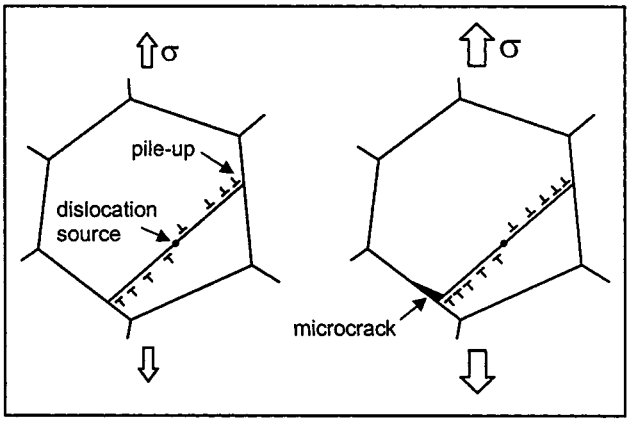

Fig. 1—An early model for cleavage fracture showing microcrack formation at the head of a dislocation pileup.

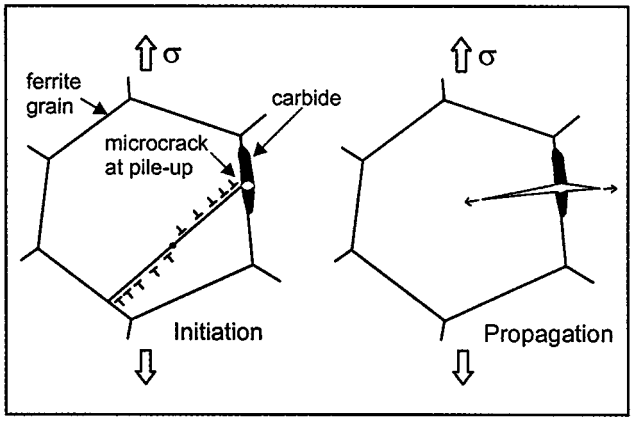

Fig. 2—The propagation control, carbide cracking model for cleavage fracture in steels.

An initial limitation of this model was its inability to explain how the events at a pileup head could create a microcrack. Zener and Stroh speculated that the dislocations may coalesce into a crack-like void, but Low[12] demonstrated that slip barriers such as grain boundaries were of insufficient strength to support pileups of the necessary intensity for microcracking. Another limitation of this model was that it could not explain why steels with a similar grain size and, therefore, similar pileup lengths displayed different cleavage resistances under certain circumstances.

B. *The Propagation-Control, Carbide-Cracking Model*

The model of Figure 1 indicates that once a crack is initiated, there is no reason for it to stop growing; *i.e.*, cleavage is initiation controlled. This, however, is inconsistent with the observation of arrested microcracks in steel toughness specimens and the apparent effect of hydrostatic stresses. On one hand, hydrostatic stresses do not influence slip and should not affect slip-operated cleavage in steels, yet hydrostatic stresses are known to promote cleavage, as demonstrated by testing progressively thicker toughness specimens. It was eventually reasoned[13,14] that hydrostatic stresses influence the cleavage process just after initiation by acting to open the microcrack (a classical stress-intensity effect), and it is generally accepted that cleavage is propagation controlled.

The idea of propagation control indicates that a sticking point (an energy barrier) exists between the initiation and propagation stages of cleavage in steel. Descriptions of this barrier were speculative until McMahon and Cohen[15] demonstrated that the cracking of cementite particles located at ferrite grain boundaries represents a primary initiation mechanism in plain carbon steels. Further study of this mechanism[16–20] lead to the model shown in Figure 2, where a carbide cracks under the influence of dislocation pileups and fibre loading. Fibre loading[20] occurs when the carbide accommodates local plastic strains in the ferrite and is stretched like a miniature tensile specimen. These strains are highest when the long dimension of the particle is parallel to the primary straining. Once the carbide snaps, the microcrack must still surmount the particle-matrix interface, an energy barrier separating initiation and propagation. Some microcracks will arrest at this point and grow no further. For the case of successful propagation, as shown in Figure 2, there is no time delay between initiation and propagation; cleavage proceeds in one continuous motion.

The addition of a cementite particle to the model of Figure 1 was a key step in cleavage studies. It provides that two steels with similar grain size can display different cleavage resistances if one contains a larger population of critically sized brittle particles.

C. *Inclusions as Cleavage Initiators*

The fact that cleavage can initiate in steels upon the fracturing of a microscopic particle suggests that any relatively brittle entity in steel is a candidate as a cleavage initiator. Nonmetallic inclusions are such, as they are brittle and present in statistically sufficient numbers. Examples of inclusion-initiated cleavage have been published,[21–25] including a few cases involving TiN inclusions.[1,26–29] For TiN inclusions, a step-by-step initiation process has been described[28,29] whereby the critical inclusion breaks* and the microcrack then surmounts key energy barriers before proceeding to the propagation stage. First, the inclusion-matrix interface is crossed, and then the nearest ferrite-ferrite grain boundary is penetrated. This description is analogous to the model shown in Figure 2.

The current article addresses additional details concerning initiation mechanics involving TiN inclusions. The subjects covered include the circumstances under which these particles break and how fractographic details can be used to understand the initiation process. Also, certain metallurgical observations are used to make inferences concerning the strength of the interface between the TiN inclusion and the ferrite matrix.

*Reference 29 also describes a cleavage initiation process that begins with the debonding of a TiN inclusion from the matrix. Results in the current study indicate that the TiN inclusions which initiate cleavage in steels do so by breakage. No evidence of initiation by debonding was found. This is not to say that TiN inclusions cannot debond. At temperatures above those at which cleavage operates, TiN inclusions can act as initiation sites for microvoid coalescence.

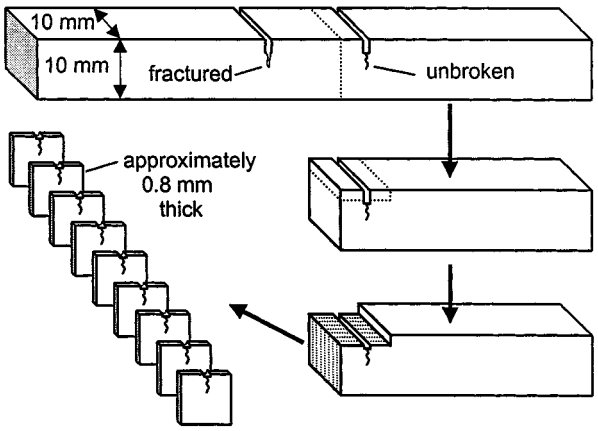

Fig. 3—The serial sectioning technique used for the double crack, four-point bend specimens.

III. EXPERIMENTAL MATERIALS AND PROCEDURES

A. *Materials*

Steel B is a commercial X-65 linepipe steel, and its chemistry and tensile properties were given in Part I of this article. This steel was microalloyed with 0.048 wt pct Ti and was thermomechanical control processed (TMCP). Steel B was acquired as a short pipe section, with a diameter of 510 mm and a wall thickness of 13 mm.

B. *Double-Crack, Four-Point Bend Tests*

Double fatigue crack, four-point bend tests were conducted to study the micromechanisms of cleavage in coarse-grain HAZ (CGHAZ) microstructures. The specimen geometry and loading configuration were shown in Part I of this article. Each specimen contained two "identical" CGHAZ areas, with fatigue precracks propagated to 50 pct of the specimen thickness. A Gleeble thermal-cycle simulator was used to generate CGHAZs representative of pipeline girth and seam welds. Thermal-cycle details were given in Part I. For each of the two CGHAZ types, approximately six specimens were tested at various temperatures between −80 °C and +10 °C.

Four-point loading subjected the crack-tip pairs in each specimen to nearly identical stresses. Unintentional, minor variations in crack length and/or local microstructure inevitably lead to cleavage initiation at one crack tip, at which time the second crack was automatically unloaded. Each specimen, therefore, produced an unfractured crack-tip volume which had been loaded to a point just prior to failure. This volume was then available for metallurgical examination, hopefully containing visual evidence of the operating cleavage mechanism. Of interest was any indication of microcracking, debonding, or other local damage associated with TiN inclusions.

Figure 3 shows how sections from the unbroken crack tips were removed for examination (hereafter called serial sectioning). The sections from each crack tip were grouped together in a single bakelite mount and polished using standard metallographic techniques. Optical microscopy was conducted in the as-polished condition at magnifications ranging from 100 to 1000 times. Once all crack-tip sections within a bakelite mount were inspected, the mount was reground/repolished. This process was repeated several times to reveal new layers deeper into each section.

C. *Scanning Electron Microscopy*

It was reported in Part I of this article that about 30 pct of the TiN inclusions contained "dark spots." These spots were hypothesized to be oxides or other inclusions on which the TiN inclusions had nucleated in the liquid steel. For Part II, additional scanning electron microscopy (SEM) work was conducted to characterize inclusion compositions. Several representative inclusions were imaged in the backscattered mode and analyzed using energy-dispersive spectroscopy (EDS). This work utilized a PHILIPS* XL 30 scanning electron microscope with a DX-4 EDAX (Energy Dispersive Analytical X-Ray) system. Polished and unetched cross sections were used to avoid EDS spectra contamination, which can occur with rough fracture surfaces. Additionally, the operating voltage was set at 10 kV to minimize interaction volume sampling of adjacent and underlying regions.

The fractography was conducted to study the features near cleavage-fracture origins. Secondary electron images were produced at an operating voltage of 20 kV. Particular attention was paid to the examination of cleavage river patterns and to the appearance of fractured inclusions found at the initiation sites.

*PHILIPS is a trademark of Philips Electronic Instruments Corp., Mahwah, NJ.

D. *Transmission Electron Microscopy*

Transmission electron microscopy (TEM) was conducted to study the inclusions that were tentatively identified in Part I as TiN. Microdiffraction was used to determine crystal structure. Bright- and dark-field imaging were used to obtain a qualitative indication of the continuity of the inclusion/matrix interface and to investigate the internal defect structure of the inclusions. The TEM work was conducted on a PHILIPS CM 200 transmission electron microscope operating at 200 kV.

Thin-foil preparation began by wet grinding 10 × 10 mm slices to a thickness of about 60 μm, using successively finer SiC papers. At this point, 3 mm discs were punched. The discs were electropolished using a twin jet unit and an electrolytic solution of 58 pct methanol, 35 pct butanol, and 7 pct perchloric acid. Polishing temperatures were maintained between −40 °C and −45 °C, and polishing voltages were varied between 45 and 52 V.

In order to obtain electron-transparent inclusions in the thin foil, it was determined that the particle had to lie within 1 or 2 μm of the hole edge. This was primarily because the matrix polished more rapidly than the inclusions, and suitably thin particles only occurred near the hole edge. To produce suitable thin foils, the following procedure was used. The electropolisher sensor that detects foil perforation was set at a high sensitivity, to indicate the first moment of hole creation. The foil was then rinsed, dried, and examined in an optical microscope at 500 times magnification. The area within about 10 to 20 μm of the hole edge was inspected for inclusions. If none were found, the foil was discarded.

If inclusions were present (typically, only one or two were present, if any) but were not at the hole edge, the foil was returned to the electropolisher and the current was applied for less than 1 second. This polishing step increased the hole diameter by a few microns. The foil was again inspected in the optical microscope. If necessary, additional polishing steps were applied. Most often, once the hole edge approached an inclusion, the particle simply fell out. Dozens of thin foils were discarded for each success.

IV. EXPERIMENTAL RESULTS

A. *Double-Crack, Four-Point Bend Tests*

Eleven crack tips were examined by the serial sectioning technique, and this produced a total of 93 crack-tip "slices." With the regrinding/repolishing steps mentioned earlier, it is estimated that about 175 crack-tip sections were examined. Several crack tips were exposed which showed TiN inclusions within close proximity to the tip itself. A total of about 10 inclusions were observed to be within about 150 μm of the tip, and several were within 50 μm.

No microcracking, debonding, or other local damage was found to be associated with the TiN inclusions located near the crack tips. This was somewhat surprising, as it was anticipated that arrested microcracks would be found in some of the TiN inclusions. Steel B was expected to show evidence of a propagation-controlled microstructure, because essentially all low-carbon, structural steels cleave by this mechanism and, therefore, subcritical (arrested) flaws should appear at brittle particles near the crack tip.

B. *SEM Inclusion Analysis*

Figure 4 shows the backscattered electron images and accompanying EDS spectra for three typical inclusions. The first inclusion image contains two areas of homogeneous atomic-number contrast: a medium-gray material (the inclusion) surrounded by a light matrix (Fe-dominated base steel). The EDS spectrum, collected using a beam centered on the inclusion, identifies the gray area as pure TiN. The barely noticeable Fe peak indicates that the steps taken to prevent X-ray contributions from areas outside the inclusion were essentially successful.

The second and third images in Figure 4 represent mixed inclusions, where the TiN material (angular in shape) surrounds a dark, "rounded" nucleus. Table I shows ZAF[30]-quantified chemical analysis for the three inclusions. The nuclei in the mixed inclusions are rich in elements lighter than Ti: primarily O, Ca, and Al. This steel was calcium treated, and a likely candidate for the nuclei material is calcium aluminate. Common formulations for this material include CA, CA_2, and CA_6, where C = CaO and A = Al_2O_3.[31]

C. *Scanning Electron Fractography*

About 25 TiN-related cleavage initiation sites were examined after being located by tracing river patterns. The two sites described here demonstrate features common to many initiation sites. The first example is of a TiN inclusion that contained a slag particle nucleus, while the second example shows a homogeneous TiN inclusion.

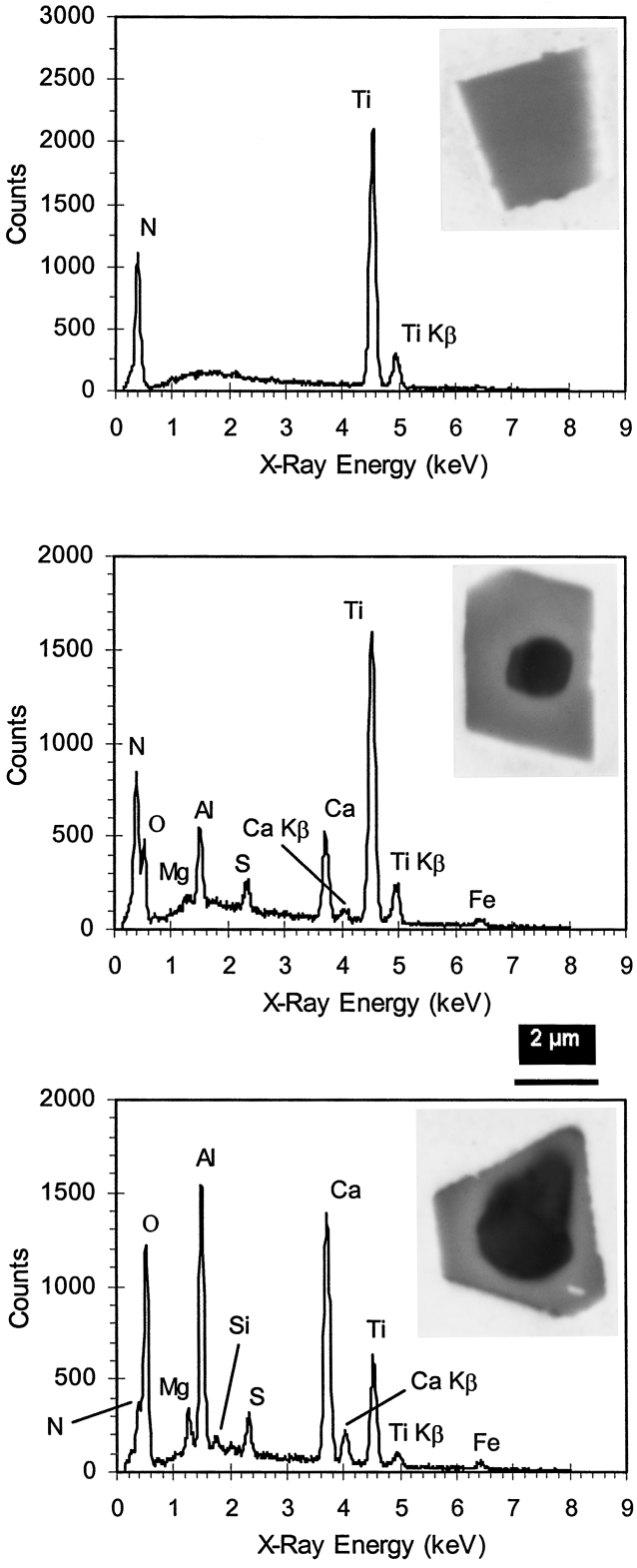

Fig. 4—Backscattered electron images and the associated EDS spectra from three types of "TiN" inclusions.

1. *First initiation-site example*

Figures 5(a) through (c) show an initiation site from a double-crack, four-point bend specimen. This specimen was processed using Gleeble program 1 (the shielded metal arc, girth-weld simulation) and tested at 0 °C. As reported in

Table I. ZAF Quantified EDS Analysis of the Inclusions in Figure 4

	Chemical Element (Wt Pct)									
TiN	Ti	N	O	Ca	Al	Mg	S	Si	P	Fe
1	83.5	13.2	—	—	—	—	—	—	—	3.2
2	50.6	11.7	20.6	7.4	3.0	0.64	1.4	—	—	4.7
3	17.2	8.1	36.4	22.6	8.7	1.5	1.7	0.31	0.25	3.2

Part I of this article, the microstructure was a mixture of about 75 pct upper bainite and 25 pct lath martensite, with an average prior-austenite grain size of 60 μm. This initiation site was located about 110 μm in front of the fatigue-crack tip. Figure 5(a) shows a large, oblong cleavage facet containing river lines that radiate from the initiating inclusion. Figures 5(b) and (c) show enlarged, mating images of the inclusion. These images can be visualized to fit together by rotating Figure 5(c) 180 deg about either of its vertical edges (flipping it upside down) and then laying it on top of Figure 5(b). Figure 6 shows the EDS spectrum from the inclusion half that is shown in Figure 5(b).

The presence of inclusion pieces in both fracture faces was confirmed by EDS, indicating that this particle fractured

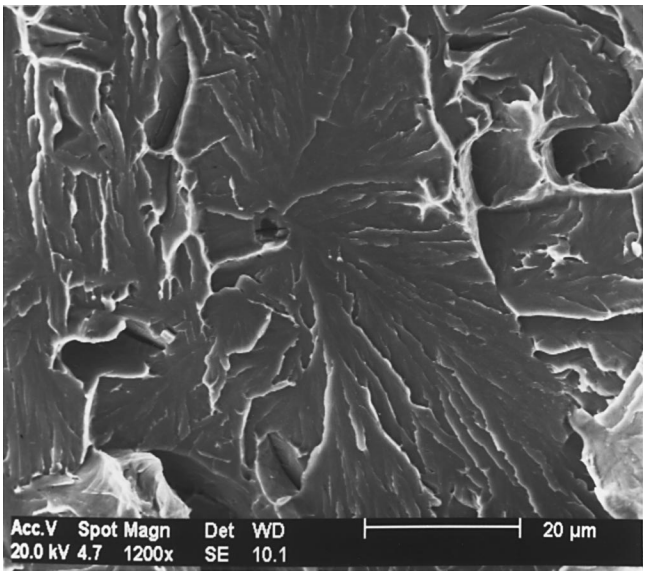

(*a*)

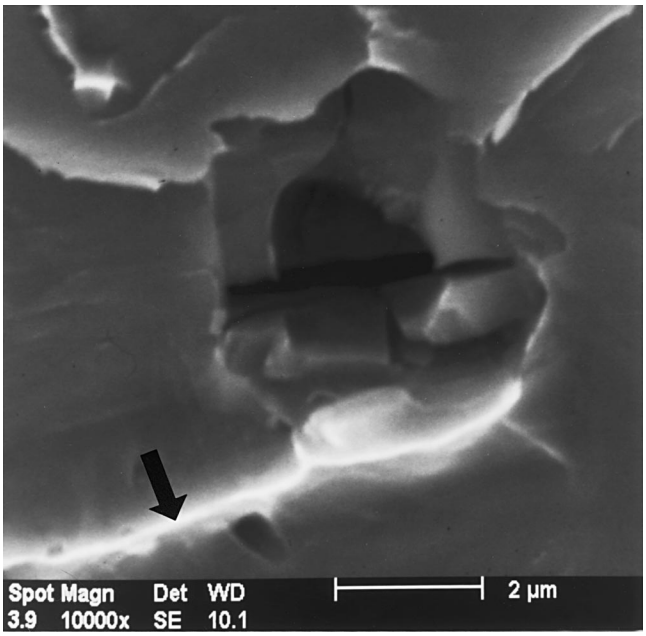

(*b*)

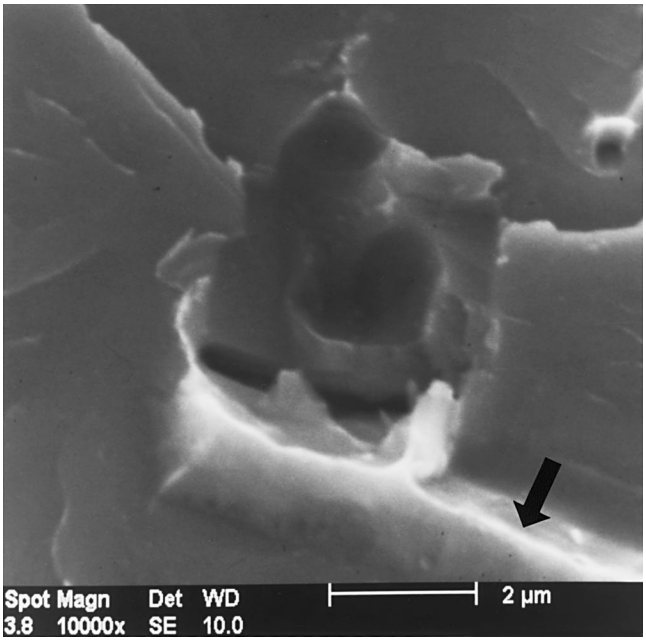

(*c*)

Fig. 5—(*a*) Scanning electron fractograph of a TiN initiation site in a four-point bend specimen. (*b*) Higher-magnification image of the TiN cleavage origin from (a). Arrow denotes tear ridge. (*c*) Mating image to the inclusion shown in (b). Arrow denotes tear ridge.

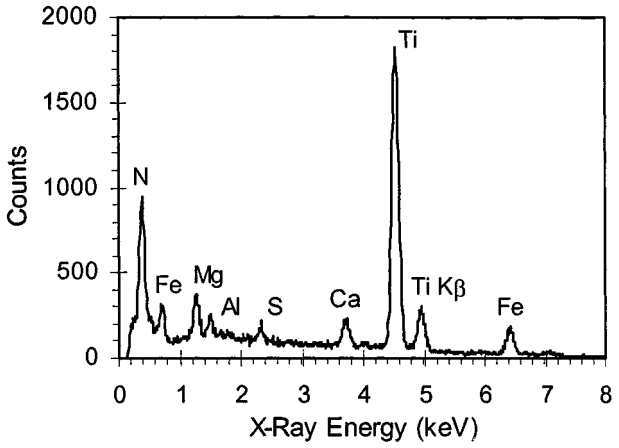

Fig. 6—EDS spectrum from the inclusion in Fig. 5(b). Peaks are $K\alpha$ unless otherwise noted.

and did not debond and pull out of the matrix. From the empty, rounded cavity in Figure 5(b) and the mating divot in Figure 5(c), it is evident this TiN inclusion contained a slag-particle nucleus that was expelled during fracture. The EDS spectrum still shows peaks (Mg, Al, S, and Ca) related to the nucleus. Of the initiation sites examined in which the TiN contained a slag-particle nucleus, the nucleus was always lost during fracture. This indicates that a relatively poor bond exists between the TiN material and the nucleus. Another common feature for this inclusion type was side cracks in the TiN material (refer to Figure 5(b) in the current article and Figure 19 in Part I). When side cracks appeared, the largest cracks were often oriented perpendicular to one another. Side cracks were never observed in the homogeneous TiN inclusions.

The river lines within the large facet shown in Figure 5(a) clearly point to the inclusion; however, they are not arranged in a perfect radial pattern with the inclusion at the center. Most of the river lines emanate from an area on the right-hand side of the inclusion. It is believed that, during initiation, the TiN microcrack transferred into the matrix through the right-hand-side and/or upper-right-hand-side inclusion-matrix boundary. With respect to this hypothesis, another interesting feature is the prominent tear ridge that intersects the lower edge of the inclusion. This ridge is identified by arrows in Figures 5(b) and (c). The significance of this ridge will be given in the discussion. Suffice it here to say that these ridge features were found at the majority of initiation sites, and they intersected the inclusions at a location opposite the side where crack transfer appeared to take place.

2. *Second initiation-site example*

One of the best examples involving a homogenous TiN inclusion was found in a notched tensile specimen that had been processed using Gleeble program 1 and tested at −20 °C. The notched tensile tests were mentioned in Part I of this article and are detailed in Reference 32. Figure 7(a) shows a low-magnification image of the tensile specimen fracture face. Tracing the river lines led to a single cleavage facet located near the specimen center (Figure 7(b)). High-magnification, mating images of the inclusion site are shown in Figures 7(c) and (d). The EDS spectrum for this TiN inclusion was essentially identical to that shown for the first inclusion in Figure 4.

Within the main cleavage facet is a particle other than the TiN initiator. This rounded and broken inclusion produced an EDS spectrum with Al, O, Ca, and Mg peaks, which is indicative of a complex oxide comprised of calcium aluminate and spinel $(MgO)(Al_2O_3)$ materials. Similar to the previous example, a prominent tear ridge appears in the main cleavage facet and runs directly into the TiN inclusion. In Figures 7(b) through (d), the tear ridge can be seen to intersect one corner of the inclusion. The river lines on the main cleavage facet point to the general area of the TiN particle; however, the river lines are biased to one side of the inclusion. As shown in Figures 7(c) and (d), the river lines emanate from the side of the TiN opposite the tear ridge. Specifically, the river lines originate from an area about 1 μm outside of the particle.

The cleavage event appears to have initiated in the TiN near the tear-ridge intersection. Along the uppermost, roughly, horizontal edge of the TiN shown in Figure 7(c), a small facet can be seen within the inclusion itself. This "flake-looking" facet mates to a depression along the analogous inclusion edge shown in Figure 7(d). This facet may have arisen due to an internal defect in the inclusion that produced a critical stress concentration (a similar facet(s) is shown in Figure 17 of Part I of this article). After microcrack initiation, it is believed that this crack traveled through the inclusion and penetrated the inclusion-matrix boundary on the side of the inclusion opposite the tear ridge. Propagation continued about 1 μm into the ferrite matrix and then burst radially in all directions. Radial propagation from the general area of the inclusion is evident in Figure 7(b).

It is hypothesized that the first instant of cleavage cracking associated with TiN inclusions is essentially unidirectional. The crack begins on one side of the inclusion, propagates to the opposite side, and then transfers into the matrix. Radial spread of the fracture does not occur until the microcrack travels a very small distance into the matrix. If this hypothesis is true, then it becomes interesting to ask why microcrack initiation would begin on one particular side of the TiN. In other words, what local phenomena would cause this directional beginning to the cleavage event?

D. *Transmission Electron Microscopy*

A relatively low-magnification TEM image of two inclusions (labeled 1 and 2) near the edge of a thin-foil hole is shown in Figure 8. A number of inclusions were examined by TEM, and the results from these two are representative of the work conducted. Microdiffraction was performed on TiN inclusion 1 to determine the crystal structure, while TiN inclusion 2 was studied for internal defects and inclusion-matrix interface continuity.

1. *Crystal structure identification*

So far, the inclusions in steel B have been referred to as TiN (implying the fcc phase); however, three structural possibilities exist within the titanium-nitrogen system:[33] (1) a Ti_2N phase having a tetragonal structure (anti-O_2Ti prototype) and narrow composition range near 33.3 at. pct N; (2) a δ' phase having a bct structure (Si_2Th prototype) and a narrow composition range near 37.5 at. pct N; and (3) a TiN phase having an fcc structure (NaCl prototype) and a wide composition range from 30 to 55 at. pct N. To determine the crystal structure of inclusion 1, the foil was

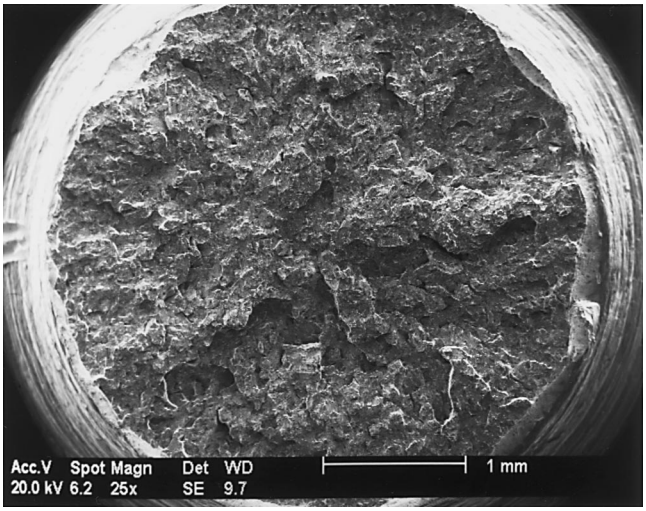

(*a*)

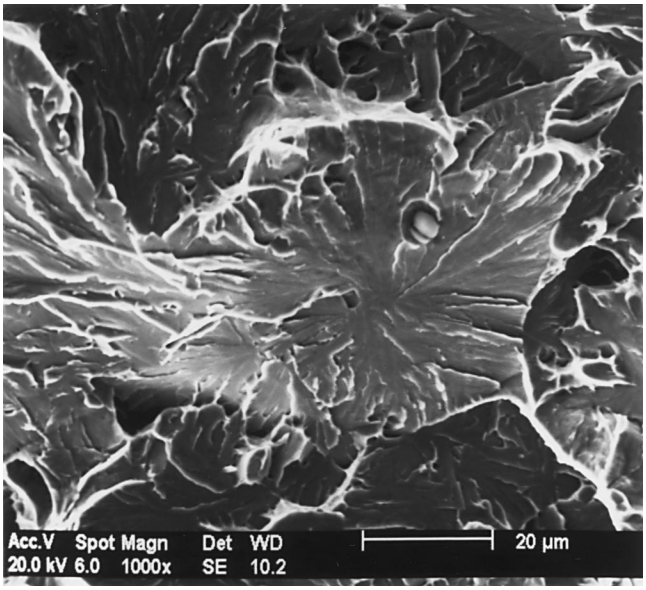

(*b*)

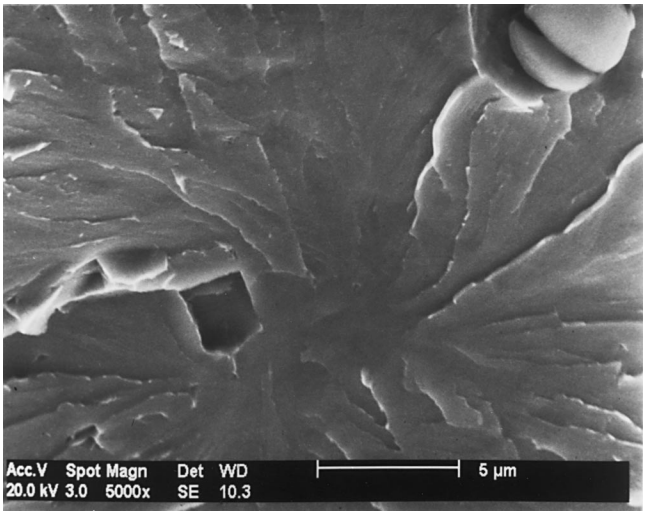

(*c*)

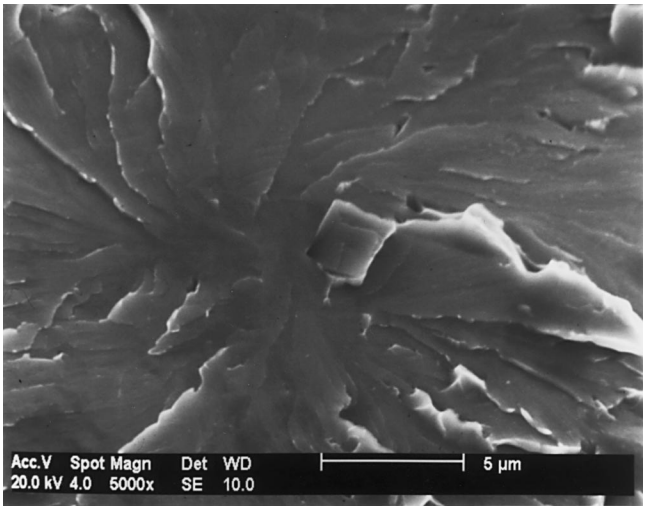

(*d*)

Fig. 7—(*a*) Scanning electron fractograph of a TiN initiation site in a notch tensile specimen. (*b*) Scanning electron fractograph of the main cleavage facet from the surface shown in (a). (*c*) Higher-magnification image of the initiation site shown in (b). (*d*) Mating image to the fractograph shown in (c).

tilted to bring various poles parallel to the beam direction, and images of the diffraction patterns were recorded. These pole patterns were compared to simulated patterns produced for the three crystal possibilities using the computer program Desktop Microscopist.[34] The diffraction patterns from inclusion 1 are most consistent with the fcc TiN phase. The negatives from four of the eight pole patterns were scanned and are shown in Figure 9, accompanied by the simulated patterns which are believed to be a match.

The lattice parameter for inclusion 1 was estimated using Eq. [1] and [2], the camera constant for the microscope, and approximately 75 spot (d) spacings measured on the diffraction pattern negatives.

$$Rd = \lambda L \qquad [1]$$

where

R = spot distance,
d = plane spacing,
λ = electron wavelength, and
L = camera length.

$$a = d\sqrt{d^2 + k^2 + l^2} \qquad [2]$$

where

a = lattice parameter, and
h, k, and l = Miller indices.

The estimated value was 4.40 Å, with a standard deviation of 0.09 Å. This value is 3.8 pct larger than the reported value of 4.24 Å[33] for pure TiN. Two reasons were considered to explain this discrepancy: (1) carbon substitution for N and (2) magnetic distortion of the spot spacings due to the steel matrix. Concerning carbon substitution, Houghton *et al.*[35] used scanning TEM (STEM) on TiN inclusions in steel to show a lattice expansion of about 0.01 Å, with a carbon

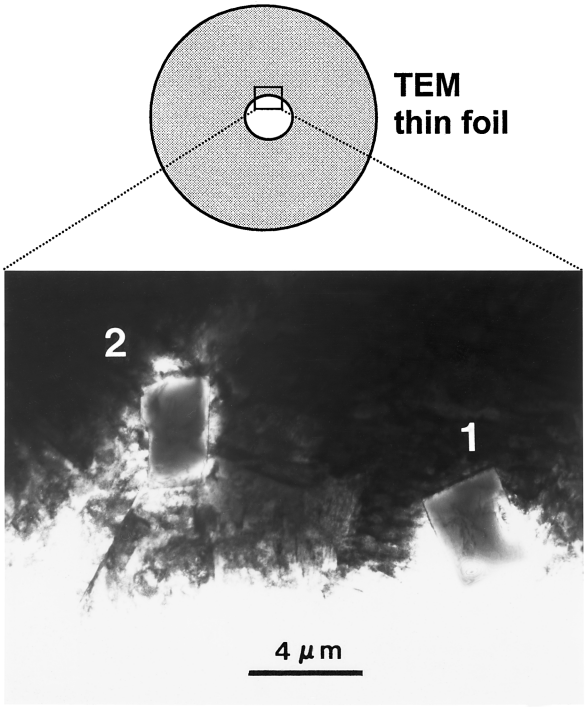

Fig. 8—Low-magnification TEM image of the edge of a thin foil hole. Two TiN inclusions are marked.

substitution of approximately 10 pct. Chen *et al.*[36] demonstrated, using electron energy-loss spectrometry (EELS) analysis on TiN inclusions in steel, that their inclusions contained essentially no C. In this study, EELS *was* able to detect both C and N in Nb-V precipitates, thus proving that if C had been present in the TiN inclusions, it would have been identified. The EELS results are significant, considering the sensitivity of this technique.

Although carbon substitution in TiN inclusions formed in steel is plausible because these particles form at high temperature in a liquid containing ample carbon, the two studies cited indicate that very little, if any, carbon substitution occurs. Also, it is worth noting that the lattice parameter of pure TiC is 4.33 Å, just 0.09 Å larger than TiN. Even if some carbon substitution in TiN did occur, it could only account for a small amount of expansion.

Concerning magnetic effects, it was noticed that considerable beam alignment and deflection problems were created by the magnetic matrix. Additionally, when comparing simulated Kikuchi maps (from Desktop Microscopist) to actual Kikuchi maps imaged by TEM, an offset in some poles by as much as 6 deg was observed. This offset orientation was always biased in the same direction. Note that about half of inclusion 1 (Figure 8) is surrounded by the ferritic (magnetic) matrix. It was concluded that the 3.8 pct discrepancy was probably due to an electron diffraction problem induced by the magnetic matrix.

2. *The inclusion-matrix interface*

No voids or gaps were observed at the inclusion-matrix interface for any of the TiN inclusions examined by TEM. Qualitatively, this indicates good interfacial continuity. Additional insights were obtained by examining the defect structure within the TiN inclusions. Figure 10 shows bright- and dark-field images of inclusion 2. Numerous dislocations are seen to exist within the inclusion itself. A number of dislocations terminate at the inclusion-matrix boundary, and a few appear to be contained entirely within the boundary. Three possibilities for the origin of these dislocations were considered. First, the dislocations may have evolved during initial particle formation (growth defects), when it nucleated and grew in the liquid steel. Second, the dislocations may have been stress induced by mechanical loading of the steel during TMCP rolling. Third, the dislocations may have been

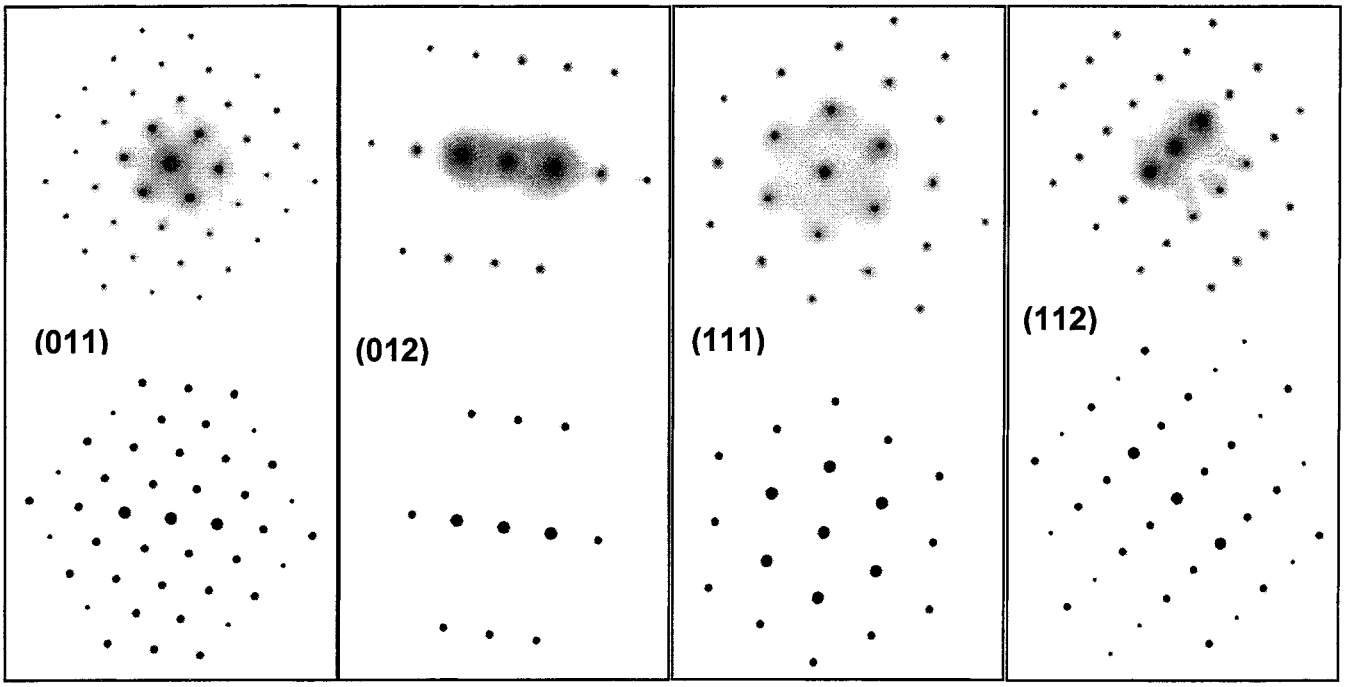

Fig. 9—The electron diffraction pole patterns associated with the TiN marked 1 in Fig. 8 are shown on top and the simulated patterns are placed at the bot tom.

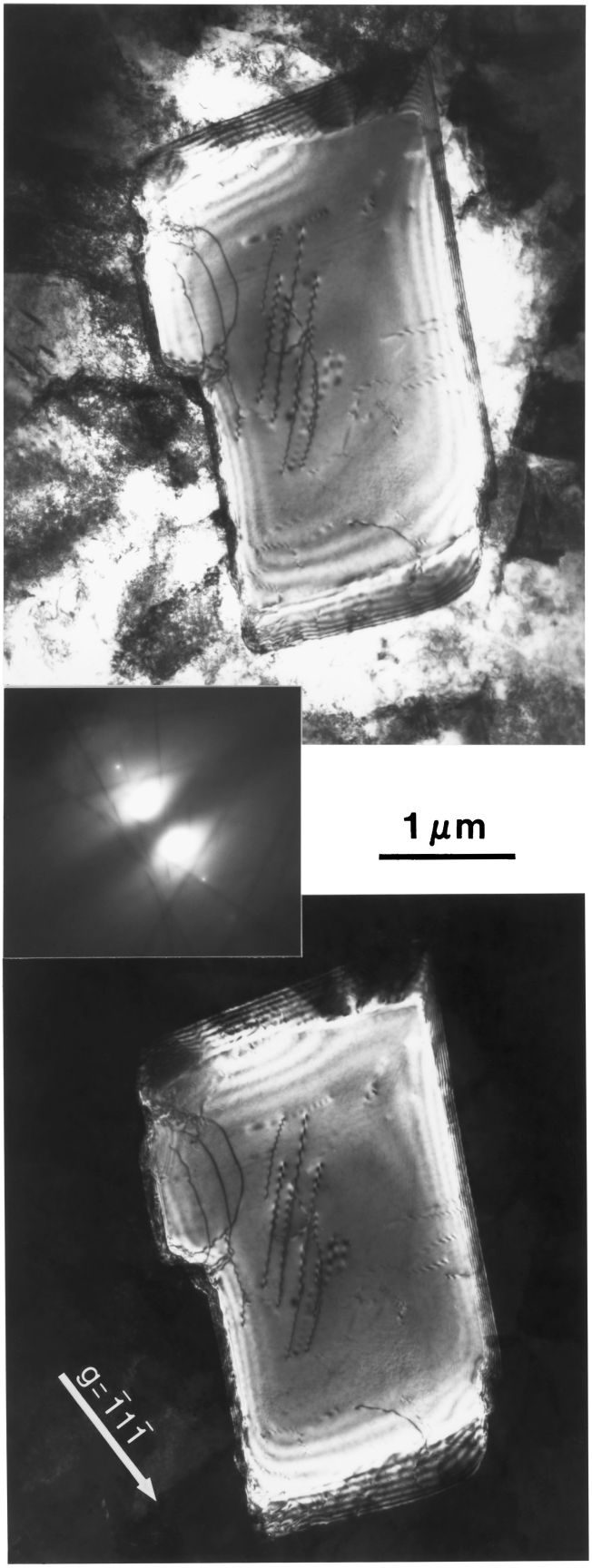

Fig. 10—Bright-field (top) and dark-field (bottom) images of the inclusion marked 2 in Fig. 8.

stress induced from the differential shrinkage between the inclusion and the matrix as the steel cooled from high temperatures. These options will be addressed in Section V.

If dislocations in TiN inclusions are stress induced, then their presence provides significant evidence of a strong inclusion-matrix bond. Creation of the dislocations by mechanical loading requires stress transfer from the matrix into the inclusion, thus indicating high interfacial strength. If the dislocations were formed as growth defects, then the phenomenon of stress transfer cannot be assumed, and no conclusions can be derived about interfacial strength.

V. DISCUSSION

A. *Estimate of Cleavage-Fracture Stress*

An estimate of cleavage-fracture stress for the fatigue-precracked, four-point bend geometry was produced using the sharp-crack, finite-element results of Nevalainen and Dodds.[37] Equations [3] and [4] relate the crack-tip principle stress($\sigma_{\theta\theta}$) to the applied J. This stress is specific to a point on the crack plane (*i.e.*, at $\theta = 0$ deg) located a distance (r) from the crack tip. The terms ε_0 and σ_0 define the proportional limit on a uniaxial stress-strain curve, and this behavior is described using a linear, then power-law, model (Eq. [5] and [6]).[37] These terms are related by $\varepsilon_0 = \sigma_0/E$.

$$\sigma_{\theta\theta} = \sigma_0 \alpha \hat{r}^{\beta} \exp(\gamma \hat{r}) \quad [3]$$

$$\hat{r} = \frac{r}{J/\sigma_0 \varepsilon_0} \quad [4]$$

$$\frac{\varepsilon}{\varepsilon_0} = \frac{\sigma}{\sigma_0} \text{ for } \varepsilon \leq \varepsilon_0 \quad [5]$$

$$\frac{\varepsilon}{\varepsilon_0} = \left(\frac{\sigma}{\sigma_0}\right)^n \text{ for } \varepsilon > \varepsilon_0 \quad [6]$$

The CGHAZ in steel B was that of a low-hardening material;[32] therefore, the finite-element results for $n = 20$ were used. This value of n set the curve-fitting parameters α, β, and γ at 2.49, −0.0476, and −6.6943, respectively.

Equations [3] and [4] are applicable for the case of small-scale yielding (SSY), *i.e.*, relative to the lower transition or lower shelf of the ductile-to-brittle transition curve. The SSY condition was verified using the relation $((W - a)\sigma_0/J) > 150$,[37] where $(W - a)$ is the ligament length (thickness minus crack length). For the four-point bend specimen of interest (described subsequently), the ligament length was 5.13 mm and the SSY verification value was 349.

Cleavage-fracture stress was estimated for the four-point bend specimen shown in Figure 17 of Part I of this article. The applied K value at failure was converted to J using the relation $J = (K_I)^2(1 - \nu^2)/E$.[37] This value of J and the distance of the initiation site from the fatigue-crack tip were substituted into Eqs. [3] and [4], thus giving a value of $\sigma_{\theta\theta}$ that was taken to be the cleavage-fracture stress σ_f. This specimen failed at an applied K value of 52.5 MPa$\sqrt{\text{m}}$, and the initiation site was located 80 μm from the crack tip. The cleavage-fracture stress was estimated to be 2150 MPa. Various values and input data for this calculation are shown in Table II.

The value of 2150 MPa compares well to two published

Table II. Calculation of Cleavage Fracture Stress

K	J	$\hat{r}$	$\sigma_{\theta\theta}$
52.5 MPa$\sqrt{\text{m}}$	12,103 J/m^2	0.0224	2150 MPa

$\varepsilon_0 = \sigma_0/E$, σ_0 = 837 MPa, E = 207,000 MPa, ν = 0.3, and r = 80 μm.

studies. Aihara and Haze[38] used crack-tip opening displacement tests on simulated CGHAZs in steels of similar composition to steel B. They were investigating martensite island–induced initiation. Although their calculation technique was somewhat different than the method presented previously, their 40 or so values of cleavage-fracture stress ranged from about 1600 to 2200 MPa. In testing simulated CGHAZs of X-65 ultralow-carbon bainitic steels, Vassilaros and Knott[26] detected cleavage initiation at TiN inclusions. Using blunt-notched bend bars at low test temperatures ($<-100\,^{\circ}$C), they calculated cleavage-fracture stresses ranging from about 1650 to 1900 MPa.

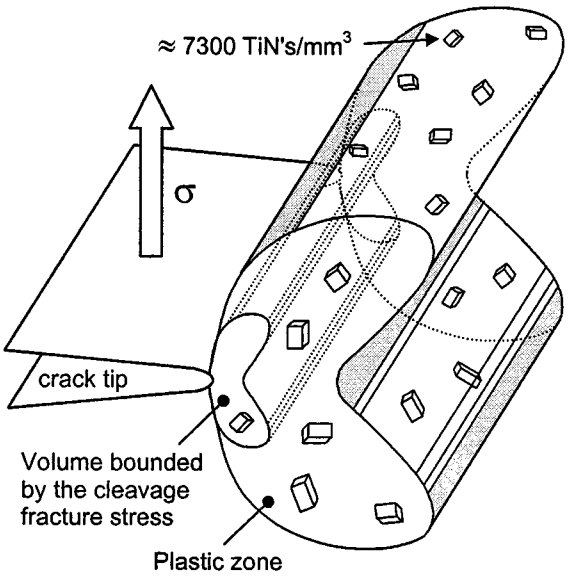

Fig. 11—Schematic of the two crack-tip contour volumes of interest.

B. *Crack-Tip Sampling of TiN Inclusions*

In a propagation-controlled microstructure where specific particles act as cleavage initiators, the particle-matrix interface represents a key energy barrier separating the initiation and propagation stages of cleavage. Microcracks that initiate in some of the particles will arrest at the interface. Arrest occurs when the driving forces responsible for microcrack growth are insufficient to overcome local material resistance. Driving forces include the dynamic energy associated with a moving crack tip and the tensile stresses that act to open the microcrack. The driving force is also influenced by particle size, as this defines microcrack size (thus, stress intensity) at the moment the tip arrives at the particle-matrix interface. Local resistance to cleavage propagation depends on several factors, including the strength of the particle-matrix interface, the orientation difference between the particle-crack plane and the matrix cleavage planes (defining how much the crack must jump or twist to enter the matrix), and the cleavage resistance of the matrix. The cleavage resistance depends significantly on the ease of local dislocation flow.

TiN inclusions were identified as the critical microstructural unit in steel B, but no evidence of arrested TiN microcracks was found during the serial sectioning of the four-point bend specimens. Possible reasons for this are (1) an insufficient number of crack-tip sections were examined, and/or (2) arrested TiN microcracks in steel B are rare. To investigate the first point, a comparison was made between the number of crack-tip TiN inclusions observed during serial sectioning *vs* an estimate of the total number of crack-tip TiN inclusions in the four-point bend specimens. This was to gain insight concerning sampling statistics; *i.e.*, is it reasonable to expect that arrested TiN microcracks can be detected by inspection of about 175 crack-tip cross sections?

The term "crack-tip TiN inclusions" refers to those inclusions that were close enough to the crack tip during testing to have cleaved. The TiN inclusions in the plastic zone are candidates, and certainly the TiN inclusions within a zone bounded by the cleavage-fracture stress would qualify. The number of inclusions in these two zones was estimated by using the number density of TiN inclusions measured in Part I of this article ($\sim$7300/mm^3), and the following calculations of crack-tip contour volumes (Eqs.[7] and [8]) for the specimen shown in Figure 17 of Part I. The contour volume for this specimen may be slightly smaller/larger than for the other ten specimens examined; however, any small error imparted by using this volume as an "average" will not affect the final conclusion. Figure 11 shows a schematic of the crack-tip volumes being considered.

Equation[7][37] allows the calculation of a crack-tip area A (a contour area) that is bounded by a principle stress σ_1. Contour area sizes are controlled, primarily, by the applied J value. The curve-fitting parameters (H_i) depend on the strain-hardening exponent (n). Using $\varepsilon_0 = \sigma_0/E$ and rearranging Eq. [7] gives Eq. [8]. These equations are applicable for SSY conditions.

$$\log_{10}\left(\frac{A\sigma_0^2\varepsilon_0^2}{J^2}\right) = \bar{A} = H_0 + H_1\left(\frac{\sigma_1}{\sigma_0}\right) + H_2\left(\frac{\sigma_1}{\sigma_0}\right)^2 + H_3\left(\frac{\sigma_1}{\sigma_0}\right)^3 + H_4\left(\frac{\sigma_1}{\sigma_0}\right)^4 \quad [7]$$

$$A = \frac{10^{\bar{A}}J^2E^2}{\sigma_0^4} \quad [8]$$

For the plastic-zone contour area, the ratio σ_1/σ_0 is approximately equal to 2, and, for the contour area bounded by the cleavage-fracture stress, $\sigma_1 = \sigma_f$ and $\sigma_f/\sigma_0 = 2.6$. The values of K, J, ε_0, σ_0, and n were the same as those used to estimate σ_f. The values of the parameters H_0 through H_4 were 2.7583, -3.5533, 0.2896, 0.3015, and -0.0875, respectively. The plastic-zone area was calculated to be 0.0848 mm^2, and the area bounded by σ_f was calculated to be 0.0089 mm^2. These areas were converted to volumes by multiplying by the specimen width (10 mm). Using 7300 TiN inclusions/mm^3, the number of TiN inclusions contained in the plastic zone and cleavage fracture stress contour volumes were estimated to be 6189 and 646, respectively.

A total of about 10 crack-tip TiN inclusions were observed in 175 cross sections. All of these TiN inclusions were within

the boundary of the plastic zone, but only about half were close enough to the crack tip (<80 μm) to have been within the cleavage fracture stress contour volume. Therefore, the serial sectioning technique exposed about 0.16 pct (*i.e.*, 10/6189) of the plastic-zone TiN inclusions and about 0.8 pct of the TiN inclusions in the cleavage-fracture stress volume. It is concluded that the number of sections examined was probably insufficient to find arrested TiN microcracks. This highlights the statistical difficulty associated with two-dimensional metallurgical investigations of crack-tip phenomena.

On the subject of rarity, the following explanation is offered. Consider the various types of particles that might initiate cleavage in a steel microstructure. TiN, Al_2O_3, and Fe_3C are three examples. Each species possesses a unique combination of mechanical properties and interfacial strength with the matrix. Within this continuum of particles, there exists a range of cleavage-initiating potencies. The least potent are inefficient in transferring microcracks into the matrix. In this case, arrested microcracks should be relatively abundant, because many failed attempts at crack transfer will likely precede the final cleavage event. On the other hand, potent initiators transfer cracks efficiently and should display a relative rarity of arrested microcracks. Fewer attempts are necessary to produce the final event. By this reasoning, and because it has been demonstrated that TiN inclusions are potent initiators, it is speculated that arrested TiN microcracks should be rare compared to other particle types.

C. *Dislocations in TiN Inclusions*

For low-carbon, structural steels, TiN inclusions nucleate in the liquid steel casting. The majority of particle growth occurs during this stage. It is conceivable that some dislocations in the TiN inclusions could form as growth defects. Formation by mechanical means at this stage can be ruled out, as no significant shear stress would be imposed on the particle by its liquid surroundings.

For structural steels similar to steel B (manufactured by TMCP), rolling of the slab/plates begins at about 1100 °C or 1200 °C. Rolling continues at successively lower temperatures, all of which are above the A_3 temperature (approximately 800 °C). High stresses are imposed on the TiN inclusions from rolling deformation and from the differential thermal contractions between the inclusions and matrix during cooling. The shrinkage stresses are referred to as tessellated stresses, a topic well documented in the literature.[31,39–42] Tessellated stresses arise from differences in the thermal-expansion coefficient. The average coefficients of linear thermal expansion, in units of 10^{-6} mm/mm/°C for austenite,[42] ferrite in mild steel,[43] and TiN,[42] are 23.0, 12.3, and 9.4, respectively. With decreasing temperature, TiN inclusions shrink less than, and are compressed by, the matrix. After the steel has cooled to ambient temperature, the TiN inclusions are in a state of residual compression. The tessellated loading can be of sufficient intensity to plastically deform the nearby matrix.[40,42]

Information concerning slip in TiN was not found in the literature; however, one source covered deformation in transition-metal carbides, including TiC,[44] and this information is expected to be relevant to TiN. The primary slip system for all NaCl-type carbides of the transition metals is the same as for fcc metals, {111}⟨110⟩. Most importantly, these carbides are incapable of slip deformation below about 800 °C because of a high Peierls stress. At such temperatures, the stress required for slip is higher than that for the competing process of cleavage, and these carbides are inherently brittle. This suggests that, for TiN inclusions in rolled steels, stress-induced dislocations would most likely be produced at high temperatures during the first few rolling passes.

Although the exact mechanism of dislocation generation in TiN inclusions is not known, the following sequence is proposed. As the particle undergoes growth in the liquid steel, the first few dislocations form as growth defects. Subsequently, these defects act as nucleation sources for dislocation production, which is driven by the stress from initial rolling and/or shrinkage of the austenite. From the standpoint of creating dislocations, the rolling stresses are probably most significant, because the tessellated stresses tend to create hydrostatic compression. Some asymmetric tessellated stresses are possible, however, if the inclusion is oddly shaped or if the local matrix is inhomogeneous.

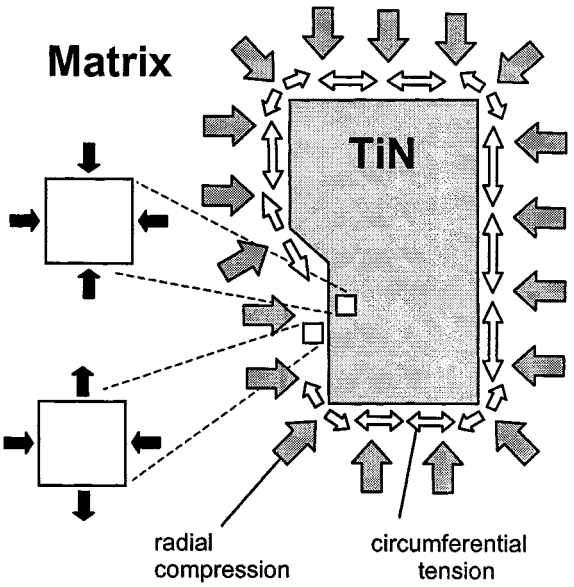

Fig. 12—Diagram showing the primary tessellated stresses associated with a TiN inclusion.

D. *Tessellated Stresses*

The tessellated stresses associated with a TiN inclusion are best referenced to a spherical coordinate system. The particle experiences radial compression, while the matrix experiences both radial compression and circumferential tension. Tensile-stress formation can be visualized by imagining stretching a small hole to fit around a larger particle. The circumference must be elongated. A schematic drawing of a tessellated stress field is shown in Figure 12. As mentioned previously, tessellated loading can plastically deform the matrix. This indicates that the tessellated residual stresses can be of, at least, yield magnitude. Tessellated stresses can significantly affect mechanical properties, and it has been reported[42] that they can be more influential than the particle-induced stress concentration that occurs during applied loading.

Tessellated stresses are believed by the authors to have

several possible effects on TiN-initiated cleavage in steels. First, the compressive stresses in the matrix provide mechanical support to the inclusion-matrix interface, thus enhancing bond strength. This protects the interface during steel processing and, upon cleavage initiation, promotes a continuous interface and efficient crack transfer. The second effect involves an elevation of propagation driving force. For particle orientations where a long side is approximately perpendicular to the crack plane, the circumferential tension will be additive to the high-magnitude stresses developed in the process zone (*i.e.*, $\sigma_{\theta\theta}$). Once a TiN microcrack penetrates the matrix, it immediately experiences tensile stresses that are elevated due to the superposition of the tessellated tension. This suggests that TiN inclusions with an oblong, basically rectangular geometry, which are oriented with their long sides nearly perpendicular to the crack plane, will be relatively more potent initiators than most other geometries/orientations. This is somewhat analogous to the fibre loading theory for cementite particles.[20]

A third possible effect involves the hydrostatic compression within the TiN itself. These stresses may provide protection against early initiation by countering the pileup impingement and/or balancing the triaxial tension that develops in the process zone. Consider the example of an engineering component undergoing applied loading, which contains a crack with a TiN inclusion near the crack tip. Hypothetically, consider that the hydrostatic compression does not exist in this TiN inclusion. For the sake of discussion, consider the magnitude of cleavage driving forces to increase with applied load in equal increments (levels) from zero to ten, where, at ten, the component would cleave by some mechanism not associated with TiN inclusions. Without the hydrostatic compression (protection), microcracking of the TiN might occur at, perhaps, level three when the driving forces are insufficient to transfer/propagate the crack into the matrix; *i.e.*, the microcrack arrests. If all TiN inclusions broke when the driving forces were too small to cause propagation, these inclusions would be benign to the steel's cleavage resistance.

Now consider the real case, where tessellated compression exists and provides some protection against the forces attempting to break the TiN inclusion. Cracking of the TiN inclusion is delayed past level three to, perhaps, level six. Although a slight toughness enhancement is anticipated (compared to the hypothetical case) because cracking takes place at higher applied loads, the likelihood of catastrophic propagation is actually higher at level six than at level three. Hydrostatic compression may delay cracking to a time when failure of TiN inclusions becomes more dangerous. Compared to inclusions with higher thermal-expansion coefficients and smaller tessellated stresses, catastrophic propagation from TiN inclusions may be more likely, because TiN inclusions may survive slightly longer in the process zone. This scenario is consistent with the hypothesis of arrested TiN microcracks being rare.

E. *Strength of the Inclusion-Matrix Interface*

It is a claim of this study that the cleavage-initiating potency of TiN inclusions is dependent on the strength of the inclusion-matrix interface. The following observations provide evidence of significant strength.

(1) The dislocations in the TiN inclusions (assuming that some are mechanically induced) imply a strong inclusion-matrix bond, a prerequisite for the stress transfer that created these defects.
(2) Depending on whether the inclusions have a larger or smaller thermal-expansion coefficient than the matrix, they can be classified as "stress raisers" or "void formers."[42] Void formers, like MnS, tend to pull away from the hole in which they reside. This accounts for the innocuous effect of MnS on fatigue properties.[42] Stress raisers, like TiN, are accompanied by compressive tesselated stresses that enhance interfacial strength.
(3) The SEM fractography and the sectioning of the four-point bend specimens revealed TiN inclusions whose matrix surroundings had experienced high plastic strains near the crack tip. Despite these strains, no debonding of the inclusions from the matrix was observed.
(4) Hundreds of cross sections of steel B were polished in preparation for optical microscopy. During final polishing, these specimens were examined at 500 times magnification for polish quality. Also, the nature and morphology of various inclusion types was studied. The appearance of the inclusions was grouped into two categories: (1) the angular/cuboidal-shaped TiN inclusions, which appeared yellow-gold in color, and (2) the rounded sulfides and oxides, which appeared dark gray or black. It was noticed that the oxides and sulfides were often pulled from the matrix, leaving empty holes and potential etch pits. In fact, they provided a primary source of scratching that necessitated regular washing of the polishing cloth. On the other hand, of the hundreds of TiN inclusions observed, not one case of pulling from the matrix was detected. It is surmised that the bond strength was responsible for the intact TiN inclusions.

F. *Directional Microcrack Initiation*

Why would a TiN microcrack initiate at a specific location in the inclusion and then propagate to the other side of the particle? A variety of possibilities exist. Microcracking in TiN inclusions is believed to be caused primarily by the impingement of dislocation pileups that form in the matrix (analogous to the model shown in Figure 2). Therefore, microcrack initiation will be more likely at the location of impingement. A second factor is that TiN inclusions are not always shaped as perfect cubes. They may have corners or ledges (Part I, Figure 8) that create local stress concentrations. A third factor concerns the observation of dislocations in TiN inclusions. These defects are sources of crystal weakness, thus making certain portions of the inclusion more susceptible to crack initiation. Other defects such as vacancies or porosity may also create local weaknesses.

Structural steels contain large numbers of nonmetallic inclusions, and the high-stress zone of the crack tip will sample a large number of cleavage-initiating candidates. The inclusion(s) that succeeds in initiating the final, catastrophic event will likely display a combination of stress-raising factors that are more severe relative to other inclusions.

G. *The Tear Ridge*

An example of a tear ridge is highlighted by arrows in Figures 5(b) and (c). Tear ridges appeared at the majority

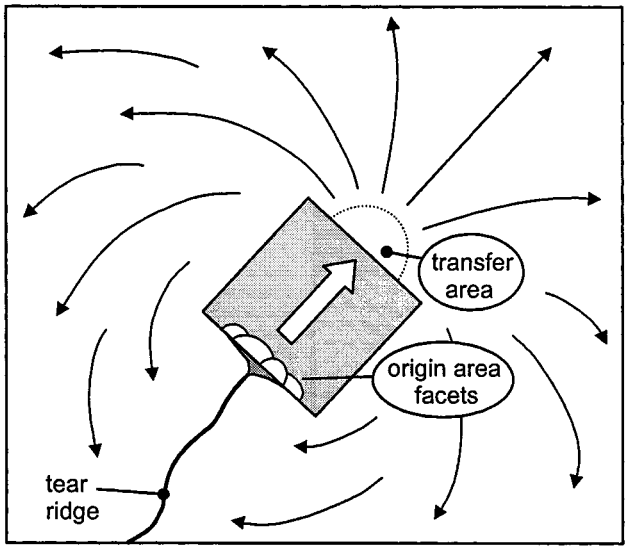

Fig. 13—Schematic showing the mechanism that forms a tear ridge.

of TiN initiation sites examined in this study. Tear ridges associated with inclusion-induced cleavage also appear in other published fractographs: Figure 11(b) of Reference 22; Figure 4(c) of Reference 24; Figures 6, 7(b), 8(b), and 9(b) of Reference 25; Figure 7 of Reference 26; and Figure 14 of Reference 29.

The mechanism that is believed to form a tear ridge is shown schematically in Figure 13. Cleavage initiates at a sensitive location in the TiN inclusion: an area where the particle is irregular in shape or contains defects. The microcrack travels to the other side of the particle and transfers into the matrix. After propagating in the matrix for a short distance (for example, 1 or 2 μm), cleavage spreads radially. Continued propagation in the general direction established by the initiation event is obvious. However, for cleavage to reach the matrix area near the fracture origin, propagation must reverse directions. This is accomplished by simultaneous propagation around both sides of the inclusion. The single crack divides into two cracks. When the cracks rejoin, they are on slightly different elevations (cleavage planes), because they have propagated through different material. A ridge of torn material defines the "rejoining" boundary.

From the standpoint of fractographic study, several aspects of cleavage can be deduced from the tear ridge. Identification of the cleavage origin can be determined more accurately. Rather than simply locating the offending particle, the ridge intersection denotes the approximate location of initiation within the particle itself. In the current study, inspection of this area revealed small facets (refer to Figures 7(c) and (d) in this article and Figure 17(d) in Part I) that are thought to be associated with initiation-influencing defects. The general direction of microcrack travel within the inclusion can be inferred to be going away from the tear-ridge intersection. The point of inclusion-to-matrix crack transfer will be located near the side of the particle opposite the tear-ridge intersection. These observations, along with high-magnification fractography, provide further understanding about cleavage initiation in steels.

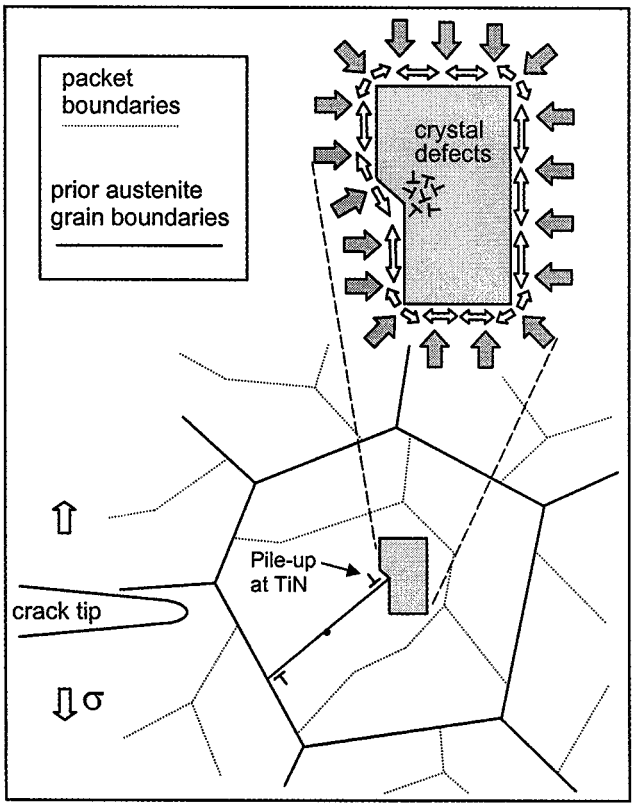

Fig. 14—Model for TiN-induced cleavage. Stage I—(early loading) a dislocation pileup impinging a sensitive area.

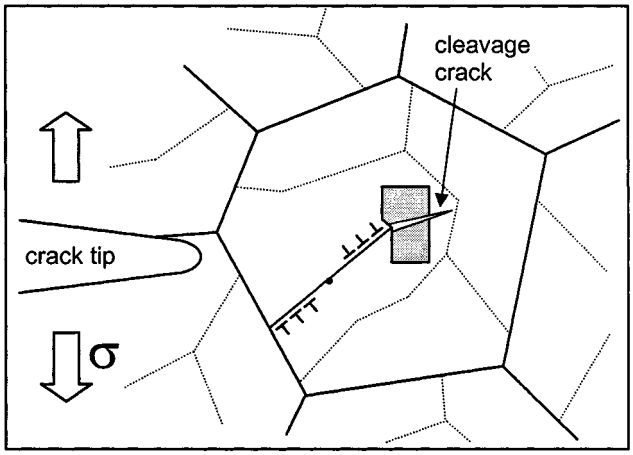

Fig. 15—Stage II—cleavage initiation at the moment of crack transfer into the matrix.

H. *A Model for Cleavage Initiation*

Based on the results from the current study, a three-stage model for TiN-induced cleavage in steels was developed and is shown in Figures 14 through 16. In the first stage (Figure 14), a TiN inclusion located near a crack tip undergoes initial loading. The microstructure in this example is that of a CGHAZ in a low-carbon, structural steel where the prior-austenite grains are subdivided into packets. Within one packet, a dislocation source is unpinned; a pileup develops and impinges the inclusion at a sensitive area. This

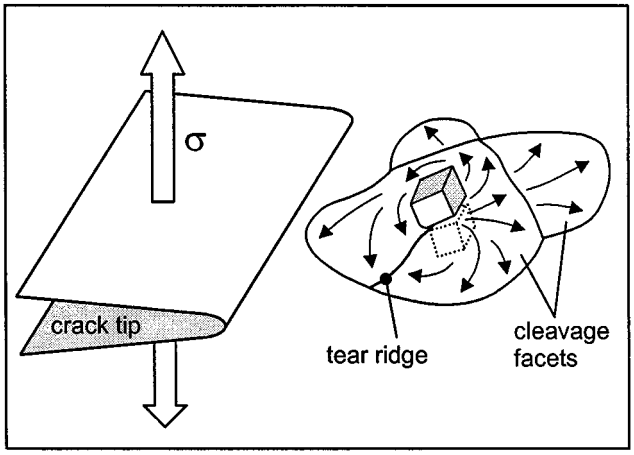

Fig. 16—Stage III—cleavage propagation showing radial spread of the fracture from the TiN and creation of the tear ridge.

area consists of a cluster of crystal defects and a surface irregularity. Although the defects in the nitride are sketched as dislocations in Figure 14, vacancies and/or porosity might also be present. Within the process zone, many other TiN inclusions (possibly hundreds or thousands) will be impinged by pileups. It is hypothesized that the critical TiN inclusion, the one that causes catastrophic cleavage, is more likely to suffer impingement at a sensitive area and/or have a "long side" oriented approximately perpendicular to the plane of the crack tip. The compressive tessellated stresses within the inclusion may provide some protection against microcracking at this stage.

The second stage is cleavage initiation (Figure 15). The applied stress increases and the pileup cracks the TiN. This crack travels across the TiN and arrives at the inclusion-matrix interface, the energy barrier separating initiation and propagation. Although the possibility of microcrack arrest exists at this point, in the case of the critical TiN inclusion, there is no hesitation between initiation and propagation. Cleavage proceeds dynamically in one continuous motion.

The third stage is cleavage propagation (Figure 16). The TiN microcrack transfers into the matrix, propagates a short distance, and then bursts radially. Continued propagation includes rotating around both sides of the inclusion, eventually rejoining, and creating a tear ridge. This transfer-and-rotation mechanism is subtly different from previous cleavage models (Figure 2), where transfer occurs simultaneously from both sides of a brittle particle.* Figure 13 can be considered to be a postcleavage, two-dimensional view of the propagation stage, as would be observed by SEM fractography.

If this cleavage model were set in a base-metal microstructure instead of a CGHAZ, then the critical energy barrier separating initiation and propagation might be the first ferrite-ferrite grain boundary beyond the inclusion-matrix interface. In the example given, the initiation event occurs within a relatively coarse microstructure (not drawn to scale), and propagation occurs more easily than in a fine-grained base metal. By the time the crack arrives at the first prior-austenite grain boundary, the cleavage driving forces are high and arrest is unlikely. This indicates that, while potent cleavage initiators like TiN inclusions can be detrimental to base metals, they are particularly deleterious to weld HAZs.

*The crack transfer mechanism shown in Figure 2 is not refuted. Fractographic evidence of this "simultaneous" mechanism is shown in Figure 8(g) of Reference 23, whereby two tear ridges emanate from the initiating inclusion.

I. *Unresolved Issues*

Two aspects concerning the cleavage-initiating potency of inclusions in steel deserve further research: (1) the comparative failure strength of inclusions while embedded in a ferrite matrix, and (2) the nature of the bond with the ferritic matrix. Although knowledge of bulk properties would provide useful information on the strength issue, it will not provide the complete answer. The property of interest is the strength of the inclusion while embedded in a ferrite matrix. Factors such as tessellated stresses, bond strength, dislocation pileups, and the ability of the matrix to transfer loads to the inclusion will play key roles. The current work indicates that the most-potent cleavage initiators may be those particles that survive some amount of initial loading (*i.e.*, are relatively strong while embedded in a ferrite matrix), but eventually fail in a brittle fashion and transfer their microcrack into the matrix with relative ease. Concerning bond strength, TiN inclusions are apparently different from many other inclusion types. Although tessellated compression will affect bond strength, other factors such as atomic attractions and registry must be considered. Additional research will enable steel metallurgists to better control casting/slagging methods and to engineer inclusions to optimize properties.

VI. CONCLUSIONS

1. The inclusions that caused cleavage initiation in steel B were identified, using electron microdiffraction, as the fcc phase (NaCl prototype) in the titanium-nitrogen system. About 30 pct of the TiN inclusions nucleated on other inclusions, which appear to be calcium aluminate.
2. Post-test examination of 175 crack-tip cross sections from four-point bend specimens revealed about 10 TiN inclusions, but no evidence of arrested TiN microcracks. It was estimated that less than 1 pct of the TiN inclusions in the plastic zone and in a region bounded by the cleavage-fracture stress were observed. The 175 sections examined were deemed too few to expect microcrack detection, thus highlighting the statistical difficulty of such work. It was also hypothesized that arrested TiN microcracks may be rare, due to their initiating potency. As compared to less-potent particles, TiN inclusions require fewer "attempts" before causing catastrophic cleavage.
3. TiN inclusions were found to contain dislocations, some of which are believed to be stress-induced during high-temperature rolling of the steel. The matrix-to-inclusion stress transfer necessary to create these defects is indicative of a strong inclusion-matrix bond, a key factor for initiation potency.
4. Tessellated stresses arising from differential thermal contraction create hydrostatic compression in the TiN and the matrix. Circumferential tension also forms in the matrix adjacent to the TiN. The compression enhances the strength of the inclusion-matrix interface. The compression may also protect the TiN during early loading and

delay initiation to a later stage, when catastrophic propagation is more likely. The circumferential tension is believed to assist propagation by increasing the stresses which open a transferred microcrack. Overall, the tessellated stresses are anticipated to increase the cleavage-initiating potency of TiN inclusions.

5. During cleavage initiation, it appears that the TiN microcrack begins on one side of the inclusion, propagates to the other side, and then transfers into the matrix. Initiation at a particular location in the particle is believed to be caused by dislocation pileup impingement and stress concentrations such as crystal defects and surface irregularities at the TiN.
6. A tear ridge accompanied essentially all cleavage-initiating TiN inclusions. A model for the creation of this feature is proposed (Figure 13). The location of the tear ridge can be used to infer where cleavage began in the TiN and where the microcrack transferred into the matrix.
7. A model for TiN-induced cleavage initiation was devised and is shown schematically in Figures 14 through 16. This model suggests that crack transfer occurs from one side, or from a local area, of the inclusion. Radial spread of cleavage requires that some of the propagation occurs in the reverse direction and rotates around the particle. This mechanism is somewhat different than that proposed in the 1960s for grain-boundary carbides, wherein a crack transfers simultaneously from two or more sides of the inclusion.

ACKNOWLEDGMENTS

This article is based on a portion of DPF's Ph.D. Dissertation and was funded by an American Welding Society Fellowship. Conversations with Drs. Malcolm Gray, Claire Davis, Peter Harrison, Shuji Aihara, and Robert Dodds are sincerely appreciated. The assistance of Hank Colijn, The Ohio State University's Campus Electron Optics facility, is gratefully acknowledged.

REFERENCES

1. D.P. Fairchild, D.G. Howden, and W.A.T. Clark: *Metall. Mater. Trans. A*, 2000, vol. 31A, pp. 641-52.
2. E. Orowan: *Rep. Progr. Phys.*, 1948, vol. 12, pp. 185-233.
3. N.J. Petch: *Progr. Met. Phys.*, 1954, vol. 5, pp. 1-52.
4. A.A. Griffith: *Phil. Trans. R. Soc. A*, 1920, vol. 221, pp. 163-98.
5. J.R. Low: *Trans. ASM*, 1954, vol. 46, pp. 163-79.
6. C. Crussard, R. Borione, J. Plateau, Y. Morillon, and F. Maratray: *J. Iron Steel Inst.*, 1956, June, pp. 146-77.
7. A.N. Stroh: *Adv. Phys.*, 1957, vol. 6, pp. 419-65.
8. C. Zener: *Trans. ASM*, 1948, vol. 40A, pp. 3-31.
9. N.F. Mott: *Proc. R. Soc. A*, 1953, vol. 220, pp. 1-14.
10. A. N. Stroh: *Proc. R. Soc. A*, 1954, vol. 223, pp. 404-14.
11. A.N. Stroh: *Proc. R. Soc. A*, 1955, vol. 232, pp. 548-60.
12. J.R. Low: *Progr. Mater. Sci.*, 1963, vol. 12, pp. 3-96.
13. A.H. Cottrell: *Trans. TMS*, 1958, Apr., pp. 192-203.
14. G.T. Hahn, W.S. Owen, B.L. Averbach, and M. Cohen: *Welding J.*, 1959, Sept., pp. 367s-376s.
15. C.J. McMahon and M. Cohen: *Acta Metall.*, 1965, vol. 13, pp. 591-604.
16. E. Smith: *Physical Basis of Yield and Fracture*, Institute of Physics and the Physical Society, Oxford Conf., Oxford, United Kingdom, 1966, pp. 36-46.
17. E. Smith: *Int. J. Fract. Mech.*, 1968, vol. 4, pp. 131-45.
18. G. Oates: *J. Iron Steel Inst.*, 1968, Sept., pp. 930-35.
19. G. Oates: *J. Iron Steel Inst.*, 1969, Mar., pp. 353-57.
20. T.C. Lindley, G. Oates, and C.E. Richards: *Acta Metall.*, 1970, vol. 18, pp. 1127-36.
21. A.R. Rosenfield, D.K. Shetty, and A.J. Skidmore: *Metall. Trans. A*, 1983, vol. 14A, pp. 1934-37.
22. J.H. Tweed and J.F. Knott: *Acta Metall.*, 1987, vol. 35, pp. 1401-14.
23. J.H. Chen and N. Yan: *Mater. Sci. Technol.*, 1988, vol. 4 (8), pp. 732-39.
24. P.L. Harrison, D.J. Abson, A.R. Jones, and D.J. Sparkes: in *Quantitative Methods in Fractography*, ASTM STP 1085, B. M. Strauss and S. K. Putatunda, eds., ASTM, Philadelphia, PA, 1990, pp. 102-22.
25. D.J. Alexander and I.M. Bernstein: *Metall. Trans. A*, 1989, vol. 20A, pp. 2321-35.
26. M.G. Vassilaros and J.F. Knott: *Proc. 3rd Int. Conf. on Trends in Welding Research*, Gatlinburg, TN, June 1–5, 1992, ASM, Materials Park, OH, 1992, pp. 519-25.
27. M.A. Linaza, J.L. Romero, J.M. Rodriguez-Ibabe, and J.J. Urcola: *Scripta Metall.*, 1993, vol. 29 (4), pp. 451-56.
28. M.A. Linaza, J.L. Romero, J.M. Rodriguez-Ibabe, and J.J. Urcola: *Scripta Metall.*, 1993, vol. 29 (9), pp. 1217-22.
29. P.L. Harrison and P.H. Bateson: *Proc. Conf. Titanium Technology in Microalloyed Steels*, The University of Sheffield, T.N. Baker, ed., The Institute of Materials, London, 1994, pp. 180-96.
30. J.I. Goldstein, D.E. Newbury, P. Echlin, D.C. Joy, C. Fiori, and E. Lifshin: *Scanning Electron Microscopy and X-Ray Microanalysis*, Plenum Press, New York, NY, 1984.
31. D. Brooksbank: *J. Iron Steel Inst.*, 1970, May, pp. 495-99.
32. D.P. Fairchild: Ph.D. Thesis, The Ohio State University, Columbus, OH, 1995.
33. *Phase Diagrams of Binary Titanium Alloys*, J.L. Murray, ed., ASM INTERNATIONAL, Materials Park, OH, 1990, pp. 176-86.
34. M.E. Schlienger and J.T. Stanley: *Desktop Microscopist*, Virtual Laboratories, Albuquerque, NM.
35. D.C. Houghton, G.C. Weatherly, and J.D. Embury: *Proc. Conf. on Thermomechanical Processing of Microalloyed Austenite*, Pittsburgh, PA, Aug. 17–19, 1981, TMS-AIME, Warrendale, PA, 1981, pp. 267-92.
36. Z. Chen, M.H. Loretto, and R.C. Cochrane: *Mater. Sci. Technol.*, 1987, vol. 3, pp. 836-44.
37. M. Nevalainen and R. H. Dodds: *Int. J. Fract. 74*, 1995, pp. 131-61.
38. S. Aihara and T. Haze: *TMS Annual Meeting*, Phoenix, AZ, Jan. 25–28, 1988, paper no. A88-14.
39. D. Brooksbank and K.W. Andrews: *J. Iron Steel Inst.*, 1968, June, pp. 595-99.
40. D. Brooksbank and K.W. Andrews: *J. Iron Steel Inst.*, 1969, Apr., pp. 474-83.
41. D. Brooksbank and K.W. Andrews: *J. Iron Steel Inst.*, 1970, June, pp. 582-86.
42. D. Brooksbank and K.W. Andrews: *J. Iron Steel Inst.*, 1972, Apr., pp. 246-55.
43. *Handbook of Chemistry and Physics*, R.C. Weast, ed., CRC Press, Cleveland, OH, 1975, p. D171.
44. L.E. Toth: *Transition Metal Carbides and Nitrides*, Academic Press Inc., New York, NY, 1971.